ORIGINAL RESEARCH ARTICLE

Ultrasonic Effect on the Deformation Behavior and Microstructure Evolution of a TRIP-Assisted Steel

JIARUI KANG and XUN LIU

The effect of ultrasonic vibration on the deformation mechanism of a TRIP-assisted steel is comprehensively studied based on micro-tensile tests. Lower flow stress and work hardening rate are observed in ultrasonically assisted (UA) conditions. Digital image correlation (DIC) analysis reveals the change in strain distribution and formation of Lüders-like deformation bands under superimposed UA. Electron backscatter diffraction (EBSD) characterization shows that at the same strain, UA reduces the fraction of retained austenite that is transformed to martensite, indicating a delayed martensitic transformation process. Additionally, EBSD reveals less low-angle grain boundaries and geometrically necessary dislocations with UA. All these microstructure modifications contribute to reduced flow stress and the change of strain distribution during deformation.

https://doi.org/10.1007/s11661-021-06398-z

I. INTRODUCTION

IN the demand of higher fuel efficiency and lower CO_2 emissions, the continuous drive for lightweight vehicles has greatly increased applications of Advanced High Strength Steels (AHSSs) and other lightweight materials in autobody structures. AHSSs generally have tensile strength of above 600MPa and maintain satisfying ductility for crash safety performance.[1] Transformation-Induced Plasticity (TRIP) steel is one group of AHSSs. It has a complex multiphase microstructure composed of ferrite matrix and a dispersion of bainite, retained austenite, and low amount of martensite. Retained austenite is metastable at room temperature and can transform to martensite during deformation. The strain associated with phase transformation increases steel plasticity, and the transformed martensite strengthens the ferrite matrix in a similar manner as to a composite.[2] These two effects lead to a prominent balance of high strength and ductility.[3] Despite the desired mechanical performance, the involved high processing force for these materials raises manufacturing challenges, especially in the field of forming. In this regard, temporary material softening aided by external energy is one of the promising solutions.[4]

Acoustic softening, which is induced by ultrasonic energy during material plastic deformation, was first discovered in 1955.[5] Superimposed ultrasonic vibrations with a frequency of 20 to 100 kHz and an amplitude around 1 to 30 μm[6] can effectively reduce material flow stress. After ultrasonic vibration is stopped, there can be either residual hardening[7,8] or softening,[9,10] depending on material systems and annealing states. Acoustic softening has been utilized in improving various forming processes, such as ultrasonically assisted (UA) deep drawing,[11] extrusion,[12] upsetting,[13] and incremental sheet forming,[14] where the reduction of forming force was consistently reported.[6]

Considerable number of studies has been performed to investigate the underlying mechanism of acoustic softening effect. In addition to stress superposition theory,[15–17] overall the phenomenon has been explained as the preferential absorption of acoustic energy by local lattice imperfections, such as vacancies, dislocations, and grain boundaries, which increases the mobility of dislocations and reduces critical resolved shear stress.[7,18] Specifically, in BCC material systems, Hoseini *et al.*[19] performed ultrasonically assisted tensile test on St52 steel and found that with the same amount of ultrasonic energy, the softening effect of UA is more significant with increasing grain size. Dutta *et al.*[20] reported a reduction of subgrain formation for a low carbon steel with in situ ultrasonic treatment during tensile tests. On the other hand, when ultrasonic vibration is applied perpendicularly to compression direction, enhancement of subgrain formation is observed in BCC molybdenum by Siu *et al.*[21] In FCC

JIARUI KANG and XUN LIU are with the EJTC, The Ohio State University, 1248 Arthur Adams Drive, Columbus, OH 43221. Contact e-mail: liu.7054@osu.edu

Manuscript submitted March 17, 2021; accepted July 12, 2021.

Published online: 23 July 2021

metals, Siu *et al.*[22] performed ultrasonic assisted compression on aluminum using a similar setup as in Reference 21 where they also observed enhancement of subgrain formation. Ahmadi *et al.*[23] conducted ultrasonically assisted tensile tests of pure aluminum and reported the flow stress reduction is more significant in samples with larger grains. On the other hand, in the ultrasonically assisted tensile tests on pure copper foils from Wang *et al.*[24] a similar magnitude in yield strength reduction was reported as grain size increases. In HCP metals, Zhou *et al.*[25] and Liu *et al.*[26] performed ultrasonically assisted compression of pure titanium. Zhou *et al.*[25] reported that deformation twinning saturation is promoted with ultrasonic vibration, which leads to residual softening. Liu *et al.*[26] observed that low ultrasonic energy would promote deformation twinning while high ultrasonic energy suppresses twinning. A similar trend was also observed by Wen *et al.*[27] when they conducted ultrasonically assisted tensile tests of AZ31 magnesium alloy.

Despite these studies on different material systems, so far, few open works have evaluated ultrasonic effects on the deformation behavior of AHSSs with their unique multiphase microstructure. The present study explores UA effect on the plastic deformation of TRIP 800 steel by ultrasonically assisted micro-tensile testing. The testing stage developed in previous work[28] is also equipped with in situ digital image correlation (DIC) capability to analyze the evolution of strain distribution during deformation. Scanning electron microscopy (SEM) and electron backscatter diffraction (EBSD) are employed for qualitative and quantitative determination of the distribution and volume fraction of different phases.

II. EXPERIMENTAL PROCEDURES

TRIP-assisted steel CR450Y780T-TR sheets were supplied by ArcelorMittal.[29] Ultrasonically assisted tensile tests were performed with a micro-tensile testing stage, where one of the tensile grips is directly mounted onto an ultrasonic transducer while the other is connected to a high-resolution linear actuator. Detailed descriptions of this tensile stage are given in Reference 28. Dogbone specimens were machined by wire electrical discharge machining (EDM) and placed in grips with matching geometry. The gauge length of dogbone specimen is 1.7 mm, which is more than one order of magnitude smaller compared to the wavelength of longitudinal ultrasonic wave in TRIP steel:

$$\lambda = 1/f\sqrt{E/\rho} = 8.2\,\text{cm} \qquad [1]$$

where f is ultrasonic frequency 20 KHz, E and ρ are the elastic modulus and density of TRIP steel and are 207 GPa and 7850 kg/m^3, respectively.[30] With this configuration, the variation of ultrasonic vibration amplitude along sample gauge is assumed to be negligible.[28]

The ultrasonic frequency and peak-to-peak amplitude were kept at 20 kHz and 1.3 μm, respectively. The tensile strain rate is 0.06/s. Two sets of experiments were performed. In the first set, ultrasonic vibration was continuously applied throughout testing. In the second set, ultrasound is applied for a short period intermittently during plastic deformation to study the transient effect of ultrasonic vibration. Prior to testing, dogbone specimens were grinded to remove surface defects from EDM and polished to 1 μm finish. Final polishing was performed using 0.05 μm colloidal silica in a vibratory polisher. Sample surface prior to testing is presented in Figure 1(a). After testing, corrugations can be observed on the polished surface due to martensitic transformation, as shown in Figure 1(b).

Optical images with differential interference contrast were taken using Olympus DP2- BSW. EBSD characterizations were performed on FEI Apreo field emission scanning electron microscope equipped with EDAX Hikari EBSD detector at 20 mm working distance, 6.4 nA beam current, and 20 kV accelerating voltage. The sample was tilted 70 deg to horizontal axis and a step size of 100 nm was used for all scans. Post processing was performed with NPAR (neighboring pattern averaging and reindexing) in OIM Analysis to improve signal to noise ratio. No other data cleanup was performed. All data points were indexed as austenite or α-ferrite. The slight tetragonality of martensite lattice makes it challenging to perform phase identification using Kikuchi patterns because of the similarity between martensite and ferrite. Accordingly, the separation of these phases was carried out using an image quality (IQ)-based method developed by Wilson *et al.*[31] Because of the internal strain and distortion in martensite BCT lattice, its Kikuchi pattern is diffuse and low in image quality. Grain averaged image quality map is used here as it gives minimal overlap between martensite and ferrite peaks.[32] A grey scale map of grain average IQ (IQ_{GA}) and its distribution in area fraction are provided in Figures 2(a) and (b), respectively. The dark region in Figure 2(a) with low IQ_{GA} corresponds to martensite while brighter region with high IQ_{GA} corresponds to ferrite and deformation-free austenite. The threshold value of IQ_{GA} for martensite is obtained after overlaying IQ_{GA} map with phase map so that deformed austenite is excluded. Dislocation-rich bainitic ferrite is also low in grain average IQ and is counted in martensite as a simplification. Three scans are collected on each testing condition to determine the average fractions of different phases considering measurement variations.

III. RESULTS

A. *Stress–Strain Behavior with UA*

Figure 3(a) shows the change in stress-strain response with continuous UA applied throughout the tensile test. While there is no noticeable difference in elastic regime, a 45MPa drop in yield point is observed in UA condition. The drop in flow stress increases with strain

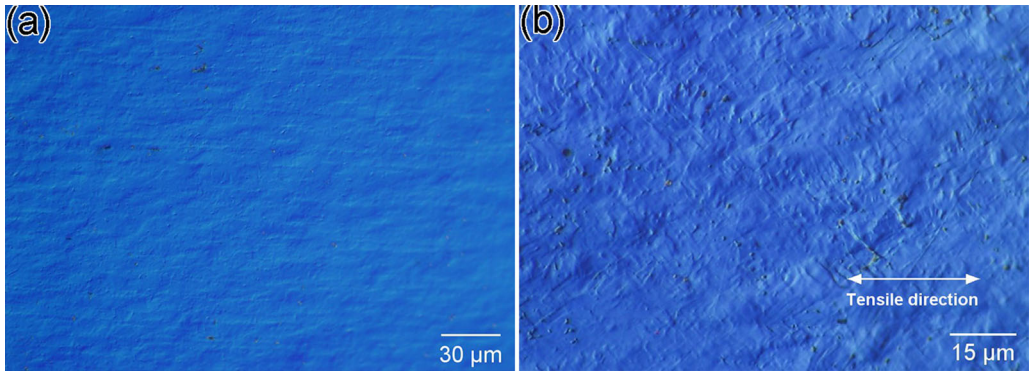

Fig. 1—Optical images of (*a*) polished TRIP 800 steel prior to testing; (*b*) deformed TRIP 800 steel with 17 pct tensile strain.

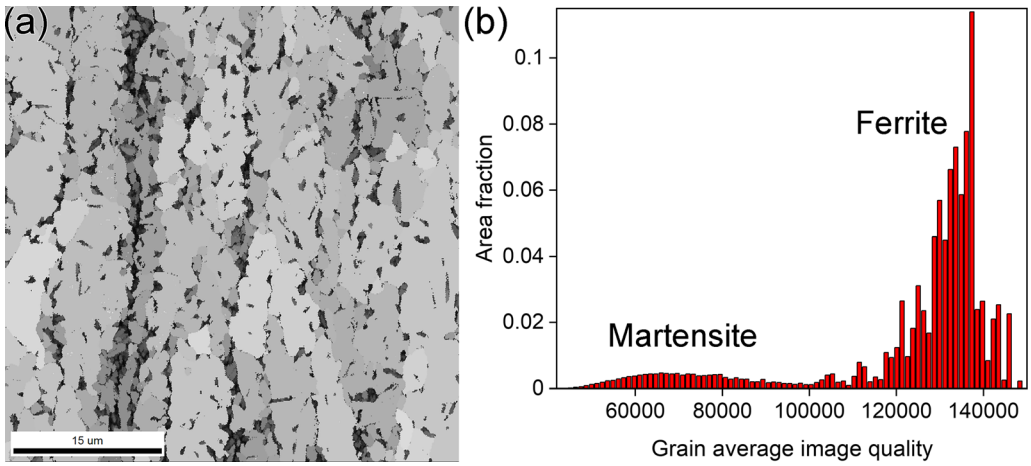

Fig. 2—Microstructure of TRIP 800 steel (*a*) grain averaged image quality map; (*b*) distribution of grain average image quality.

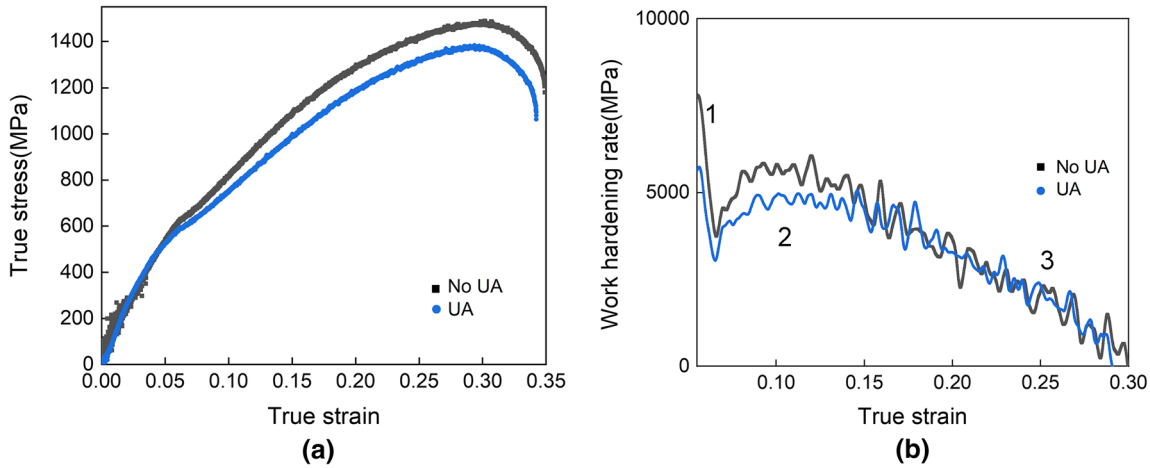

Fig. 3—Tensile test of TRIP 800 with continuous UA (*a*) true stress-strain curve; (*b*) work hardening rate.

as the specimen with UA hardens at a lower rate. The maximum reduction in flow stress is around 100MPa. To compare the influence of UA on work hardening, work hardening rate $d\sigma/d\varepsilon$ of true stress-strain curves are calculated and plotted in Figure 3(b). The change of work hardening rate can be characterized into three stages during tensile test of a TRIP-assisted steel. During the first stage of plastic deformation, hardening rate decreases considerably, which is associated with the deformation of ferrite and austenite.[33,34] TRIP effect occurs in the second stage that follows,[35] where work hardening rate increases, as shown in Figure 3(b). In the last stage, work hardening rate decreases monotonically till necking. The hardening rate of UA sample is lower

than the one without UA in the first two stages, especially in stage 2. Since stage 2 is closely related to TRIP effect, it is inferred that martensitic transformation is suppressed with ultrasonic vibration starting from this stage.

Another set of tests where UA is intermittently turned on for a short period was also performed to study the dynamic effect of UA on the onset of plastic deformation. Engineering stress-strain curves are plotted and compared with the test performed in the absence of UA, as shown in Figure 4. A yield plateau that lasts for 1 pct engineering strain is observed when UA is initiated at around the yielding point of TRIP 800. The region where UA is turned on and off, illustrated in a red dashed square, was zoomed in, and presented in Figure 4 to show more details. After the yield plateau in UA specimen, flow stress stays at a lower level compared with the conventionally tested sample until UA is turned off. An average flow stress reduction of approximately 35MPa was observed.

B. *DIC Analysis*

DIC analyses were performed to investigate the evolution of strain distribution around yield plateau of the intermittent UA test shown in Figure 4. Three frames in chronological order were selected, *i.e.*, before, during, and after yield plateau, marked as frame i, ii, and iii in Figure 4. The distribution of ε_{xx} (x being tensile direction) in conventional tested as well as UA tested sample of these frames are compared in Figure 5. While no pronounced difference in strain distribution is observed at frame i, as shown in Figures 5(a) and (b) for conventional and UA sample, DIC results of frame ii are quite different. Without UA, higher strain builds up in a broad region in the middle of gauge section (Figure 5(c)), while in UA condition, as shown in Figure 5(d), localized strain can be observed at both ends of gauge section, as marked in red dash line. In comparison, after yield plateau at frame iii, the difference in strain distribution can no longer be observed, as shown in Figures 5(e) and (f). During yield plateau, UA induces the formation of Lüders-like deformation bands.[36–38] This agrees with lower hardening rate in stage 2, which results in local deformation instability.[39] The DIC result here is different from a classical Lüders band morphology and is in the appearance of simultaneous multiple Lüders bands.[40]

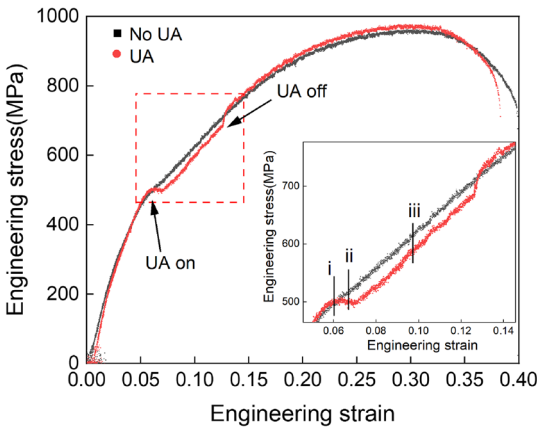

Fig. 4—Engineering stress-strain curves of TRIP 800 steel without UA and with intermittent UA.

C. *Microstructural Characterization*

1. *Enhanced austenite stability with UA*

EBSD characterizations were conducted on as-received TRIP-assisted steel, samples tested to 5 and 17 pct engineering strain with and without UA. Phase maps were reconstructed and presented in Figure 6, where banding of both austenite and martensite from cold-rolling can be observed.[41,42] Figure 6(a) shows the phase distribution of undeformed TRIP-assisted steel, where only 1.1 pct martensite is present. Deformed samples with 5 pct strain, 5 pct strain UA, 17 pct strain, and 17 pct strain UA are shown in Figure 6(b) through (e), respectively.

Percentages of these phases in different conditions are compared in Figure 7. With increasing strain, more austenite transforms to martensite. The average percentage of austenite decreases from 8.2 pct in as-received condition to 6.2 and 3.9 pct with 5 and 17 pct strain, respectively. When investigating the effect of UA, little insight can be gained by comparing the absolute values of austenite or martensite percentage due to the variation among scanned regions. As a normalization, transformed austenite is calculated as martensite fraction divided by the sum of austenite and martensite fractions, *i.e.*, the austenite fraction prior to phase transformation. With UA, transformed austenite decreased from 56.7 to 52.0 pct with 5 pct strain. The trend also holds true for 17 pct strained samples. Transformed austenite is 64.5 pct in conventional test compared to 60.4 pct with UA. This suggests that martensitic transformation is suppressed, and the stability of austenite is increased under superimposed ultrasonic energy.

In addition to chemical composition and grain size, the mechanical stability of austenite depends on the orientation of individual grain with respect to loading direction.[43] This can be described by Schmid factor m, which relates macroscopic tensile loading σ to critical resolved shear stress τ on a specific slip system:

$$\tau = m\sigma = \sigma\cos(\lambda)\cos(\varphi) \qquad [2]$$

where λ and φ are the angles between loading direction to slip plane normal and slip direction, respectively. It is well documented that austenite grains with high Schmid factor are least stable and preferentially transform to martensite under loading.[43–45] Austenite Schmid factor maps calculated from EBSD data are shown in Figure 8. Undeformed sample as well as deformed samples with 5 pct strain, 5 pct strain UA, 17 pct strain, and 17 pct strain UA are shown in Figures 8(a) through (e), respectively.

Figure 9 compares the distribution of Schmid factor in different testing conditions. Difference in the

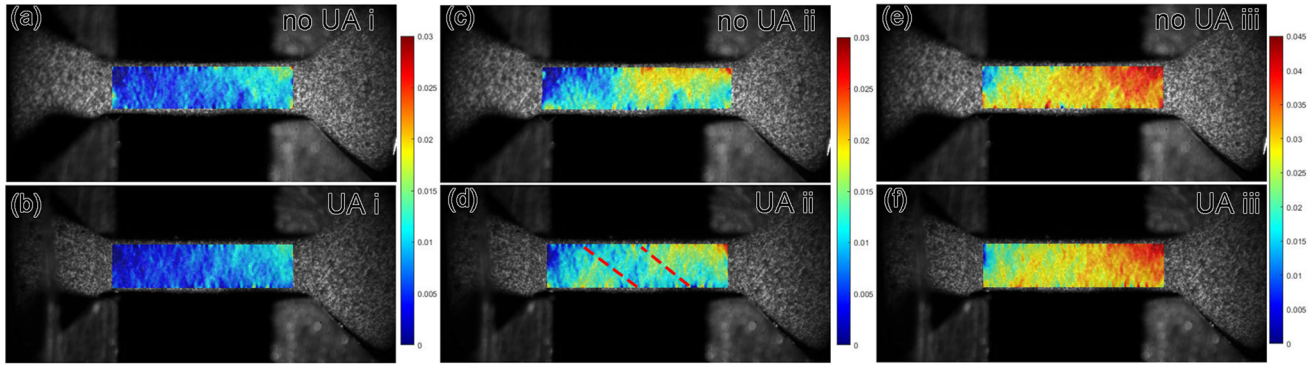

Fig. 5—Distribution of ε_{xx} at frame i (*a*) without UA, (*b*) with UA; ε_{xx} at frame ii (*c*) without UA, (*d*) with UA; and frame iii (*e*) without UA, (*f*) with UA.

distribution of Schmid factor with UA can be observed, especially at high Schmid factor regime. In 5 pct strained sample with UA, the fraction of austenite grains with Schmid factor above 0.45 decreases with increasing Schmid factor. In contrast, the opposite trend is observed in the conventionally tested sample. In fact, Schmid factor distribution for 5 pct strain with UA resembles the undeformed sample, which agrees with the results in Figure 7 showing less martensitic transformation with UA and again indicates delayed phase transformation. Similar conclusion can be drawn from the change of Schmid factor with UA in 17 pct strained samples, even though slightly higher fraction in high Schmid factor regime is observed. This is because at 17 pct strain, more than half of the retained austenite has already transformed to martensite, as shown in Figure 7. This leaves less amount of high Schmid factor austenite grains in the conventionally tested sample and higher amount of unstable austenite grains in the UA sample to be transformed to martensite. In other words, the austenite grains with higher Schmid factor in UA sample are those that are originally unstable and would have transformed to martensite without the influence of UA.

2. *Grain boundary and dislocation structure*

Figure 10 compares the distribution of grain boundary structure and geometrically necessary dislocation (GND) in different conditions. Figures 10(a) through (e) show the grain boundary maps of undeformed, 5 pct strain, 5 pct strain with UA, 17 pct strain, and 17 pct strain with UA, respectively. The corresponding GND density maps are presented in Figures 10(f) through (j). Localized GND can be observed in martensite and austenite regions.

While the number of low-angle grain boundaries (LAGBs), which is colored in red and green, is very low in undeformed sample, it increases gradually with strain. More LAGBs form as dislocations rearrangement and regrouping take place to partly release the strain energy accumulated during plastic deformation.[20] A considerable decrease in LAGB length can be noticed when comparing UA samples with the regular ones at the same strain level, as shown in Figure 11. With UA, the average length of LAGB drops from 2.71 to 1.95 mm at 5 pct strain, and from 4.38 to 3.87 mm at 17 pct strain. GNDs are stored during plastic deformation and directly related to the gradient in local misorientation. Here GND density maps are generated with the maximum misorientation angle set to 5 deg so that the points on grain boundaries are excluded in calculation. Prior to deformation, GND density is low with an average of $219.0 \times 10^{12}/m^2$. The hot spots in GND map closely follow phase boundaries, especially martensite/ferrite phase boundaries, which agrees with the observation in dual-phase steel from Calcagnotto *et al.*[46] that the GND density near ferrite/martensite interface is an order of magnitude higher than other regions. During plastic deformation, yielding is initiated first in ferrite grains, followed by austenite. The local strain gradient and strain discontinuity facilitates the transformation of austenite. The rise in GND density is attributed to the local plastic deformation gradient in ferrite matrix to accommodate the change in volume as austenite transforms to martensite. This effect is more pronounced in deformed samples as martensitic transformation progresses with increasing strain. It is noteworthy that the average density of GND drops significantly with UA, by 10.8 and 14.3 pct at 5 pct strain and 17 pct strain, respectively. The reduction in GND density is most clearly seen in ferrite matrix. This can be explained by higher dislocation mobility under oscillating stress wave. Dislocations can travel longer distances and the chance for dipole annihilation is increased.[20] Ultrasonic effect in reducing the amount of dislocation has been proposed as one of the main mechanisms for the softening behavior observed in many material systems.[6] Enhanced dislocation

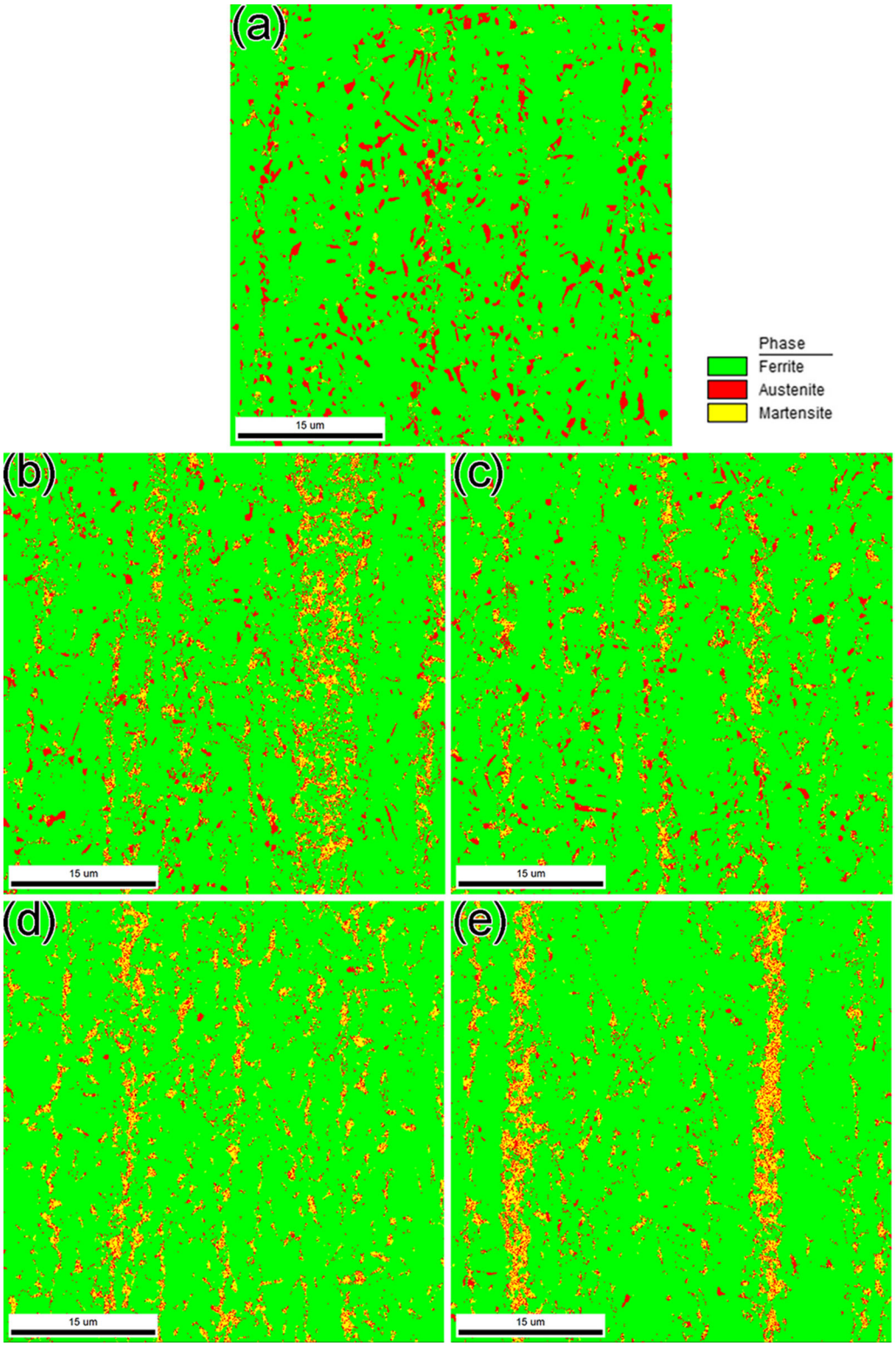

Fig. 6—Reconstructed phase maps of TRIP 800 (*a*) undeformed; (*b*) 5 pct strain; (*c*) 5 pct strain with UA; (*d*) 17 pct strain; (*e*) 17 pct strain with UA.

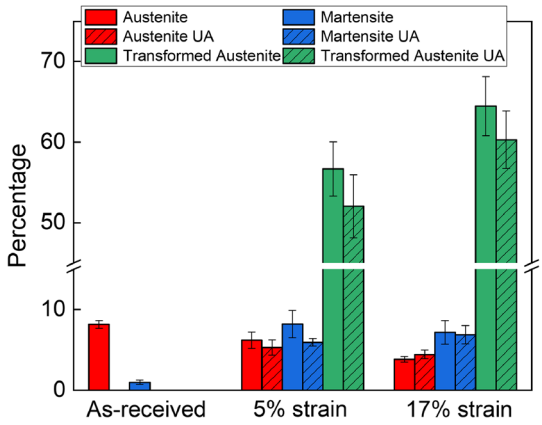

Fig. 7—Percentages of austenite, martensite and transformed austenite in different conditions.

annihilation as well as delayed martensitic transformation both contributes to the lower hardening rate and flow stress observed in ultrasonically assisted conditions.

IV. DISCUSSION

A. *The Formation of Lüders Band with UA*

Lüders-like deformation bands can be observed in UA condition during stress plateau, where higher strain initiated near the two edges of specimen gauge. In contrary, this behavior of strain distribution evolution is hardly noticeable in the conventional tensile test where strain increases more uniformly. It is known that Lüders band represents local plastic instability, and its formation is related to low work hardening rate.[39] During conventional tensile tests, the cold rolled TRIP-assisted steel did not exhibit such behavior as the strain hardening from martensitic transformation prohibits local strain from rising and homogenizes global deformation.[47] On the other hand, if martensite formation is delayed with ultrasonic assistance, heterogenous deformation would occur from the effect of Cottrell atmosphere. Similar observations of higher Lüders strain with more stabilized austenite have also been reported, where austenite can be stabilized through refined grains,[48,49] increased cold-rolling thickness reduction,[39] the amount of pre-strain[50] or chemical composition, especially carbon concentration.[51] Furthermore, the overall lower dislocation density in UA samples leads to low work hardening rate, which also promotes Lüders band formation. It should also be noted that the dominant micro-constituent of the TRIP-assisted steel in this study is ferrite, where much of the plastic strain is partitioned into. The Lüders band formation mechanisms discussed here focus on the deformation of ferrite phase instead of retained austenite. It is worth noting that stress plateau and Lüders-like deformation bands are not observed in the testing where UA is present during elastic deformation, as shown in Figure 3(a). This is attributed to the UA effect in elastic regime, where dislocation motion is observed in metal with existing defects.[52]

B. *Delayed Martensite Formation with Ultrasonic Vibration*

The delayed martensite formation with UA can be rationalized from both energy and deformation mechanism perspectives. Figure 12 illustrates the change of Gibbs free energy of austenite and martensite as a function of temperature.[53,54] T_0 is the equilibrium temperature where the Gibbs free energies of these two phases are equal. As temperature decreases, the chemical driving force for phase transformation increases. At martensite start temperature M_S, difference in the Gibbs free energy between these phases reaches the sufficient value $\Delta G_{M_s}^{\gamma\to\alpha'}$ for spontaneous martensitic transformation. Between M_S and T_0, the chemical-free energy $\Delta G_{T_1}^{\gamma\to\alpha'}$ alone is inadequate to drive martensitic transformation[55] and additional mechanical energy U needs to be supplied such that:

$$\Delta G_{T_1}^{\gamma\to\alpha'} + U = \Delta G_{M_s}^{\gamma\to\alpha'} \quad [3]$$

The mechanical energy U can be written as:

$$U = \tau\gamma + \sigma\varepsilon \quad [4]$$

where the first term represents the work done by resolved shear stress and the latter by normal stress.[56] With the application of ultrasonic vibration, flow stress is reduced and therefore the resolved shear stress and normal stress are lowered. Accordingly, to obtain the equal amount of supplement mechanical energy, a higher strain is needed. Therefore, martensitic transformation is delayed to a later stage of plastic deformation. In other words, at the same strain level, the percentage of martensite formation is smaller in ultrasonically assisted conditions.

In a TRIP-assisted steel, martensitic transformation can be either stress induced, or strain induced. As shown in Figure 12, when temperature increases from M_S to T_0, the required amount of mechanical energy to trigger martensitic transformation increases as the chemical driving force decreases. Below M_s^σ, an applied stress lower than the yield strength of austenite is capable to initiate the transformation, which corresponds to stress-induced transformation. In the temperature region between M_s^σ and M_d, the applied stress to initiate phase transformation exceeds the yield strength of austenite, resulting in the plastic deformation of austenite. This corresponds to strain-induced transformation. For commercialized TRIP-assisted steel utilized in automotive industry, M_s^σ is generally designed to be below room temperature. Accordingly, at room

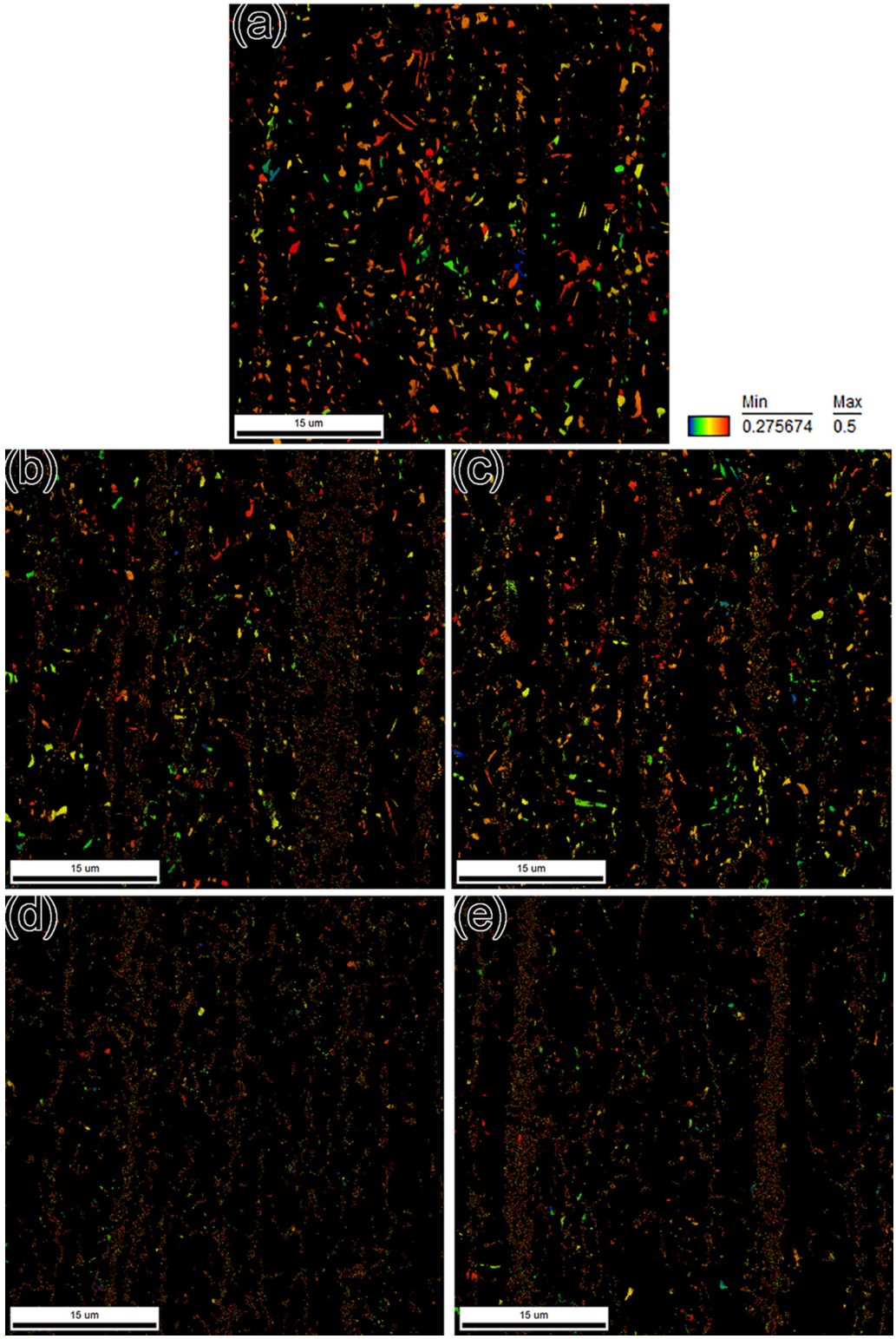

Fig. 8—Austenite Schmid factor maps of TRIP 800 (*a*) undeformed; (*b*) 5 pct strain; (*c*) 5 pct strain with UA; (*d*) 17 pct strain; (*e*) 17 pct strain with UA.

temperature, martensitic transformation is strain induced, which provides better ductility compared to stress-induced transformation. During strain-induced martensitic transformation, locations with high dislocation intersections, *i.e.*, microscopic shear bands, serve as martensite nucleation sites.[2,57,58] A smaller number of martensite embryos are available with UA as less dislocations are present in ferrite and retained

austenite. Therefore, martensitic transformation is delayed.

V. CONCLUSION

In this study, the effect of ultrasonic vibration on the deformation mechanism of a TRIP-assisted steel is comprehensively discussed based on the results from micro-tensile tests and microstructure characterizations. Consistent flow stress reduction is observed in both intermittent and continuous ultrasonically assisted tensile tests. Furthermore, in the continuous UA tested condition, the overall work hardening rate is lower. In situ DIC analyses reveal a modified strain distribution with UA, where Lüders-like deformation bands are observed. This indicates UA delays martensitic transformation, which is further confirmed by EBSD results. At the same strain level, UA reduces the percentage of

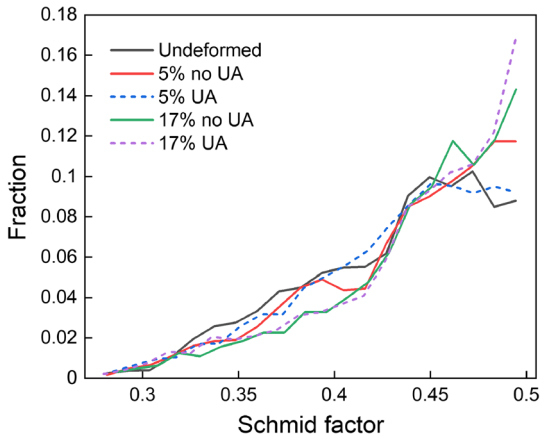

Fig. 9—Distribution of austenite Schmid factor in different conditions.

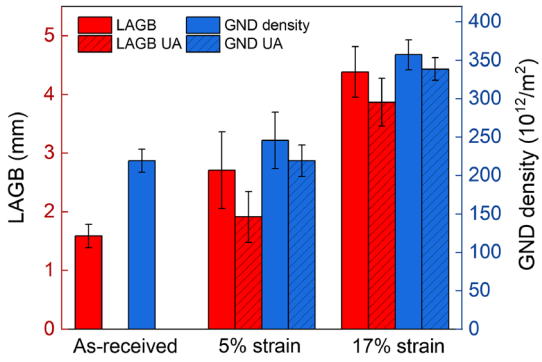

Fig. 11—LAGB and GND results in different conditions.

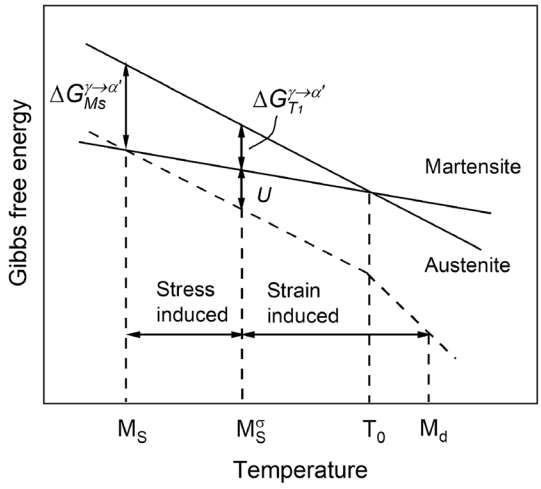

Fig. 12—Variation of martensite and austenite Gibbs free energy with temperature (Figure adapted with permission from Ref. [54]).

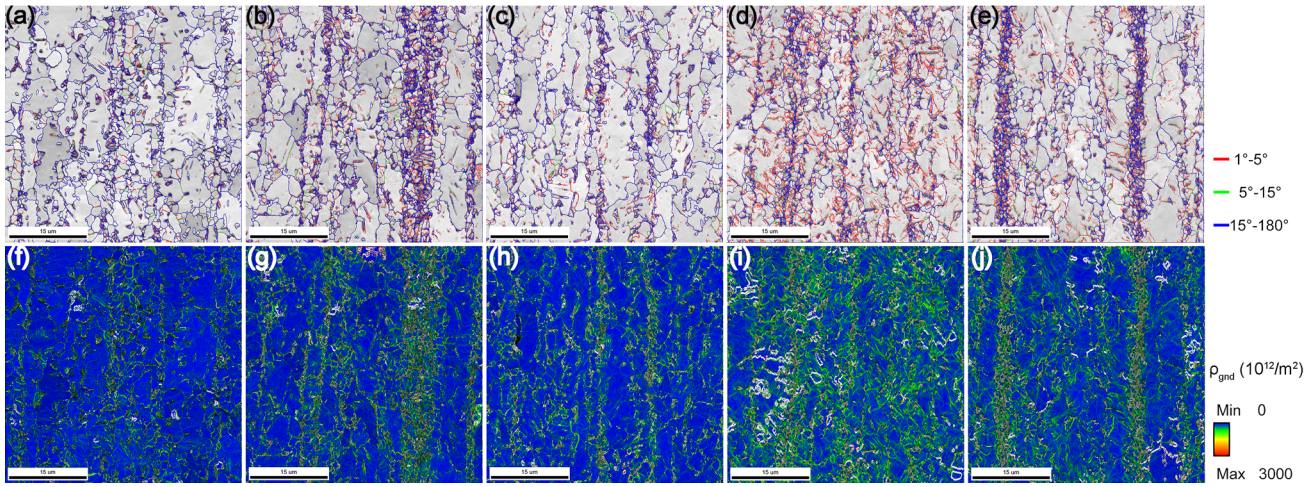

Fig. 10—EBSD boundary maps of different testing condition (*a*) undeformed; (*b*) 5 pct strain; (*c*) 5 pct strain with UA; (*d*) 17 pct strain; (*e*) 17 pct strain with UA; (*f*) through (*j*) GND maps of (a) through (e).

transformed austenite. Furthermore, EBSD shows less low-angle grain boundaries and geometrically necessary dislocations with UA, which is attributed to enhanced dislocation annihilation under oscillating ultrasonic stress. This also contributes to lower work hardening rate observed in tensile stress-strain curves. The delayed martensite formation is attributed to the reduction in supplementary mechanical energy for phase transformation because of the lowered flow stresses with UA. In addition, less available martensite nucleation sites due to the reduction of dislocation density with UA also contributes to delayed martensite formation.

ACKNOWLEDGMENTS

This work was supported by National Science Foundation CMMI AM program [Grant Number: 2019238]. Electron microscopy was performed at the Center for Electron Microscopy and Analysis (CEMAS) at The Ohio State University.

CONFLICT OF INTEREST

On behalf of all authors, the corresponding author states that there is no conflict of interest.

REFERENCES

1. O. Bouaziz, H. Zurob, and M. Huang: *Steel Res. Int*., 2013, vol. 84, pp. 937–47.
2. M.J. Sohrabi, M. Naghizadeh, and H. Mirzadeh: *Arch. Civ. Mech. Eng*., 2020, vol. 20, p. 124.
3. P.J. Jacques, Q. Furnémont, F. Lani, T. Pardoen, and F. Delannay: *Acta Mater*., 2007, vol. 55, pp. 3681–93.
4. S. Kumar, C.S. Wu, G.K. Padhy, and W. Ding: *J. Manuf. Process*., 2017, vol. 26, pp. 295–322.
5. F. Blaha and B. Langenecker: *Naturwissenschaften*, 1955, vol. 42, pp. 1–10.
6. K.F. Graff:Ultrasonic Metal Forming: Materials in *Power Ultrasonics*, J.A. Gallego-Juárez and K.F. Graff, eds., Woodhead Publishing, Oxford, 2015, pp. 337–76.
7. B. Langenecker: *IEEE Trans. Sonics Ultrason*., 1966, vol. 13, pp. 1–8.
8. N.A. Tyapunina, V.V. Blagoveshchenskii, G.M. Zinenkova, and Y.A. Ivashkin: *Sov. Phys. J*., 1982, vol. 25, pp. 569–78.
9. H. Huang, A. Pequegnat, B.H. Chang, M. Mayer, D. Du, and Y. Zhou: *J. Appl. Phys*., 2009, vol. 106, p. 113514.
10. I. Lum, H. Huang, B.H. Chang, M. Mayer, D. Du, and Y. Zhou: *J. Appl. Phys*., 2009, vol. 105, p. 024905.
11. T. Jimma, Y. Kasuga, N. Iwaki, O. Miyazawa, E. Mori, K. Ito, and H. Hatano: *J. Mater. Process. Technol*., 1998, vols. 80–81, pp. 406–12.
12. C. Bunget and G. Ngaile: *Ultrasonics*, 2011, vol. 51, pp. 606–16.
13. J-C. Hung and C. Hung: *Ultrasonics*, 2005, vol. 43, pp. 692–98.
14. R. Cheng, N. Wiley, M. Short, X. Liu, and A. Taub: *Procedia Manuf*., 2019, vol. 34, pp. 186–92.
15. G.A. Malygin: *Phys. Solid State*, 2000, vol. 42, pp. 72–78.
16. G.E. Nevill: *Effect of vibrations on the yield strength of a low carbon steel*, Rice University, 1957.
17. H.O.K. Kirchner, W.K. Kromp, F.B. Prinz, and P. Trimmel: *Mater. Sci. Eng*., 1985, vol. 68, pp. 197–206.
18. Y. Daud, M. Lucas, and Z. Huang: *J. Mater. Process. Technol*., 2007, vol. 186, pp. 179–90.
19. M. Hoseini, M. Shalvandi, and A. Salimiasl: *Modares Mech. Eng*., 2018, vol. 18, pp. 40–45.
20. R.K. Dutta, R.H. Petrov, R. Delhez, M.J.M. Hermans, I.M. Richardson, and A.J. Böttger: *Acta Mater*., 2013, vol. 61, pp. 1592–1602.
21. K.W. Siu and A.H.W. Ngan: *Mater. Sci. Eng. A*, 2013, vol. 572, pp. 56–64.
22. K.W. Siu, A.H.W. Ngan, and I.P. Jones: *Int. J. Plast*., 2011, vol. 27, pp. 788–800.
23. F. Ahmadi, M. Farzin, and M. Mandegari: *Ultrasonics*, 2015, vol. 63, pp. 111–17.
24. C.J. Wang, Y. Liu, B. Guo, D.B. Shan, and B. Zhang: *Mater. Des*., 2016, vol. 112, pp. 246–53.
25. H. Zhou, H. Cui, and Q.H. Qin: *J. Mater. Process. Technol*., 2018, vol. 251, pp. 146–59.
26. T. Liu, J. Lin, Y. Guan, Z. Xie, L. Zhu, and J. Zhai: *Ultrasonics*, 2018, vol. 89, pp. 26–33.
27. T. Wen, L. Wei, X. Chen, and C. Pei: *Int. J. Miner. Metall. Mater*., 2011, vol. 18, pp. 70–76.
28. J. Kang, X. Liu, and M. Xu: *Mater. Sci. Eng. A*, 2020, vol. 785, p. 139364.
29. ArcelorMittal: TRIP (TRansformation Induced Plasticity) steels, https://automotive.arcelormittal.com/products/flat/first_gen_AHSS/TRIP. Accessed 23 June 2021.
30. H. Li, G. Sun, G. Li, Z. Gong, D. Liu, and Q. Li: *Mater. Des*., 2011, vol. 32, pp. 3272–79.
31. A.W. Wilson, J.D. Madison, and G. Spanos: *Scripta Mater*., 2001, vol. 45, pp. 1335–40.
32. M.M. Nowell, S.I. Wright, and J.O. Carpenter: *in Materials Processing and Texture*, John Wiley & Sons, Inc., Hoboken, NJ, 2008, pp. 285–92.
33. J. Shi, X. Sun, M. Wang, W. Hui, H. Dong, and W. Cao: *Scripta Mater*., 2010, vol. 63, pp. 815–18.
34. L. Luo, W. Li, L. Wang, S. Zhou, and X. Jin: *Mater. Sci. Eng. A*, 2017, vol. 682, pp. 698–703.
35. Z.H. Cai, H. Ding, R.D.K. Misra, and Z.Y. Ying: *Acta Mater*., 2015, vol. 84, pp. 229–36.
36. X.G. Wang, L. Wang, and M.X. Huang: *Mater. Sci. Eng. A*, 2016, vol. 674, pp. 59–63.
37. M. Zhang, R. Li, J. Ding, H. Chen, J-S. Park, J. Almer, and Y-D. Wang: *Mater. Res. Lett*., 2018, vol. 6, pp. 662–67.
38. Y. Zhang and H. Ding: *Mater. Sci. Eng. A*, 2018, vol. 733, pp. 220–23.
39. H. Wang, Y. Zhang, G. Yuan, J. Kang, Y. Wang, R.D.K. Misra, and G. Wang: *Mater. Sci. Eng. A*, 2018, vol. 737, pp. 176–81.
40. T. Brlić, S. Rešković, F. Vodopivec, and I. Jandrlić: *Metalurgija*, 2018, vol. 57, pp. 357–59.
41. S.J. Kim, C.G. Lee, I. Choi, and S. Lee: *Metall. Mater. Trans. A Phys. Metall. Mater. Sci*., 2001, vol. 32, pp. 505–14.
42. K. Lee, J.H. Ryu, S.W. Lee, W.H. Lee, J.I. Kim, and D.W. Suh: *Metall. Mater. Trans. A Phys. Metall. Mater. Sci*., 2016, vol. 47, pp. 5259–65.
43. C.H. Seo, K.H. Kwon, K. Choi, K.H. Kim, J.H. Kwak, S. Lee, and N.J. Kim: *Scripta Mater*., 2012, vol. 66, pp. 519–22.
44. R. Blondé, E. Jimenez-Melero, L. Zhao, J.P. Wright, E. Brück, S. Van Der Zwaag, and N.H. Van Dijk: *Acta Mater*., 2012, vol. 60, pp. 565–77.
45. Y.B. Xu, Y. Zou, Z.P. Hu, D.T. Han, S.Q. Chen, and R.D.K. Misra: *Mater. Sci. Eng. A*, 2017, vol. 698, pp. 126–35.
46. M. Calcagnotto, D. Ponge, E. Demir, and D. Raabe: *Mater. Sci. Eng. A*, 2010, vol. 527, pp. 2738–46.
47. Y. Sakuma, D.K. Matlock, and G. Krauss: *Metall. Trans. A*, 1992, vol. 23, pp. 1221–32.
48. J.H. Ryu, J.I. Kim, H.S. Kim, C-S. Oh, H.K.D.H. Bhadeshia, and D-W. Suh: *Scripta Mater*., 2013, vol. 68, pp. 933–36.
49. M. Naghizadeh and H. Mirzadeh: *Steel Res. Int*., 2019, vol. 90, p. 1900153.
50. Z.C. Li, H. Ding, R.D.K. Misra, and Z.H. Cai: *Mater. Sci. Eng. A*, 2017, vol. 679, pp. 230–39.
51. E. Emadoddin, A. Akbarzadeh, and G.H. Daneshi: *Mater. Sci. Eng. A*, 2007, vol. 447, pp. 174–79.
52. C. Chisholm, H. Bei, M.B. Lowry, J. Oh, S.A. Syed Asif, O.L. Warren, Z.W. Shan, E.P. George, and A.M. Minor: *Acta Mater*., 2012, vol. 60, pp. 2258–64.

53. Y. Tomita and T. Iwamoto: *Int. J. Mech. Sci.*, 1995, vol. 37, pp. 1295–1305.
54. S. Curtze, V.T. Kuokkala, M. Hokka, and P. Peura: *Mater. Sci. Eng. A*, 2009, vol. 507, pp. 124–31.
55. X. Liu, S. Lan, and J. Ni: *Mater. Sci. Eng. A*, 2013, vol. 582, pp. 211–18.
56. J.R. Patel and M. Cohen: *Acta Metall.*, 1953, vol. 1, pp. 531–38.
57. T. Suzuki, H. Kojima, K. Suzuki, T. Hashimoto, S. Koike, and M. Ichihara: *Scripta Metall.*, 1976, vol. 10, pp. 353–58.
58. E. Cakmak, H. Choo, K. An, and Y. Ren: *Acta Mater.*, 2012, vol. 60, pp. 6703–13.